Ionization-density-dependent Scintillation Pulse Shape and Mechanism of Luminescence Quenching in $LaBr_3$:Ce

Jirong Cang,[1,2] XinChao Fang,[1,2] Zhi Zeng,[1,2] Ming Zeng,[*,1,2] Yinong Liu,[1,2] Zhigang Sun,[3] and Ziyun Chen[4]

[1] *Key Laboratory of Particle & Radiation Imaging, Tsinghua University, Ministry of Education, Beijing, China*
[2] *Department of Engineering Physics, Tsinghua University, Beijing 100084, China*
[3] *Institute of Materials Science & Chemical Engineering, Ningbo University, Ningbo 315211, China*
[4] *School of Electric Information & Electrical Engineering, Shanghai Jiao Tong University, Shanghai 200240, China*

(Received 7 September 2020; accepted 2 December 2020; published 29 December 2020)

Pulse-shape discrimination (PSD) is usually achieved using the different fast and slow decay components of inorganic scintillators, such as BaF_2, CsI:Tl, etc. However, $LaBr_3$:Ce is considered to not possess different components at room temperature, but has been proved to have the capability of discriminating γ and α events using fast digitizers. In this paper, ionization-density-dependent transport and rate equations are used to quantitatively model the competing processes in a particle track. With one parameter set, the model reproduces the nonproportionality response of electrons or α particles, and explains the measured α and γ pulse-shape difference well. In particular, the nonlinear quenching of excited dopant ions, Ce^{3+}, is confirmed herein to mainly contribute observable ionization α and γ pulse-shape differences. Further study of the luminescence quenching can also help to better understand the fundamental physics of nonlinear quenching and thus improve the crystal engineering. Moreover, based on the mechanism of dopant quenching, the ionization-density-dependent pulse-shape differences in other fast single-decay-component inorganic scintillators, such as lutetium yttrium oxyorthosilicate, $Lu_{2(1-x)}Y_{2x}SiO_5$:Ce (LYSO) and $CeBr_3$, are also predicted and verified with experiments.

DOI: 10.1103/PhysRevApplied.14.064075

I. INTRODUCTION

Inorganic scintillators have been widely used to monitor γ and x rays or particle beams in applications of medical imaging and dosimetry, security checks, high-energy physics, and the high-tech industry. One may hope to discover and/or engineer a scintillator with both a high light yield, high-energy resolution, small nonproportionality, and fast rise and decay times. Nonproportionality is departure from proportional response of the number of scintillation photons produced versus energy of the primary particle, which has long been considered as a fundamental limitation of the intrinsic energy resolution of scintillators [1–6]. Great efforts in both experimental measurements [7–10] and theoretical models [2,11–18] have been made to study the nonproportionality of inorganic scintillators. It is generally considered that nonproportionality arises from the variation in excitation densities depending partly on the particle energy. It is thought that high excitation densities lead to strong particle-particle interactions and nonlinear quenching and that, at low excitation densities, slow thermalization can lead to extensive charge separation [12,13,18]. Moreover, the ionization-density-dependent scintillation processes can not lead only to the nonproportionality of the scintillation yield to incident particle energy, but also the differences of pulse shapes to incident particle energy, e.g., CsI:Tl [19], or different types of particles, e.g., *n* and γ discrimination. It looks like the nonproportionality and pulse-shape differences are connected at the level of nonlinear interactions and details of transport, which may provide a basis for using the underlying extra information in pulse shape to correct the nonproportionality and thus improve the energy resolution [20].

The best scintillation performance in terms of light yield (70 000 photons/MeV), decay time (approximately 16 ns), and energy resolution (approximately 2.6% at 662 keV) has been achieved for $LaBr_3$:Ce. In recent years, many research groups, including us, have studied the α and γ pulse-shape discrimination (PSD) in $LaBr_3$:Ce crystals, but contradictory results were achieved [21–28]. It is usually considered that scintillators with multicomponent decay curves can have the ability of PSD between γ rays and massive (for example, proton and α) particles. However,

---

[*] zengming@tsinghua.edu.cn

© 2020 American Physical Society

$LaBr_3$:Ce is considered to possess only a single-decay component, but has been proved to have the capability of discriminating γ and α events using fast digitizers at room temperature, which can be used to reduce the intrinsic α background from ^{227}Ac contamination and improve its application for low-activity γ-ray spectroscopy. The physical mechanism of such a PSD capability of $LaBr_3$:Ce has remained unclear. Such pulse-shape difference, as well as strong quenching of α particles, in $LaBr_3$:Ce was generally explained to be the exciton-exciton annihilation (bimolecular decay) [29,30]. However, the precisely measured rise time, associated with self-trapped excitons, of $LaBr_3$:5%Ce pulse shape is as fast as approximately 1 ns [31], which seems not enough to cause such a small but significant difference. A complete and quantitative model illustrating the scintillation mechanism of $LaBr_3$:Ce is still needed.

The model in this paper is based on the coupled rate and transfer equations proposed by Lu *et al.* [13,14], which include most of the already known scintillation processes and has been applied to CsI:Tl crystals to explain the nonproportionality and energy-dependent pulse shapes of γ rays. Regarding the classification of inorganic scintillators, $LaBr_3$:Ce belongs to the multivalent halide [32] and shows different characters from alkali halide, such as CsI, NaI. Coupled rate and transport equations describing the main physical processes of $LaBr_3$:Ce crystal, at room temperature, are established. The model computes the evolution of excitations (including electrons, holes, excitons, and excited dopant ions) over time and space in electron tracks by solving coupled rate and transport equations describing both the movement and the linear and nonlinear interactions of the excitations along the ionization track. The tracks are initially very narrow before hot and thermalized carrier diffusion takes effect. A cylindrical Gaussian radial profile with a track radius of $r_0(\sim 3\,\mathrm{nm})$ is generally adopted to describe the distributions of excitations on a series of small cells along the ionization track as reviewed in Ref. [33]. The initial ionization density values vary from cell to cell along the track with the variation in linear energy deposition rate dE/dx and the model calculate the local light yield, of which the weighted average is the light yield, for each local value of dE/dx. Besides the light yield output, the evolution of excitations (emission intensity) over time is also responsible for the pulse shapes, which allows us to validate the model more thoroughly. Furthermore, α particle is also an alternative way to reach even higher density of excitation than that of electrons, which can be used to study and validate the ionization-density-dependent physical processes even further. The study of the scintillation mechanism of inorganic scintillators will not only help to understand the characteristics of scintillators, but also guide the optimization of alternative scintillator materials and the development of other radiation detection methods.

II. THE MODEL AND ITS PARAMETERS IN PARTICLE TRACKS

A. The scintillation mechanism in $LaBr_3$:Ce

Many studies about the properties of $LaBr_3$:Ce have been carried out and form the basis of the scintillation mechanism. X-ray excited-emission spectra of $LaBr_3$:Ce at 125 K shows that both self-trapped-exciton (STE) broad-band and double-peaked $5d\rightarrow 4f$ cerium emission are observed. The contribution of the STE broad band decreases from 70% to 37% to 8% for a Ce concentration of 0.2%, 0.5%, and 5%, respectively, which shows an antirelation between the STE emission and Ce concentration. Moreover, the emission spectra for $LaBr_3$:5%Ce, at room temperature, only arises from the double-peaked $5d\rightarrow 4f$ cerium emission [34]. The scintillation time profiles measured with a delayed coincidence method or a time-correlated single-photon counting (TCSPC) method reveal more information about the scintillation mechanism of $LaBr_3$:Ce. Although STEs do not contribute the emission directly, at room temperature, according to the emission spectra of $LaBr_3$:Ce, Glodo *et al.* [35] suggested a diffusion and energy transfer model of STEs to Ce based on the linear relation between the logarithms of Ce concentration and rise time of scintillation time profiles [35]. Later on, Bizarri and Dorenbos proposed a STE-transport-based model to account for γ-excited luminescence in $LaBr_3$ with different Ce concentrations and at different temperatures [36]. In that model, three processes are proposed, i.e., (i) process I, the prompt sequential capture of electron and holes by Ce; (ii) fast process II, thermally activated energy transfer from self-trapped excitons situated in the close surrounding of a cerium ion to that cerium ion; (iii) slow process II, thermally activated migration of STEs over a distance to encounter a Ce dopant followed by energy transfer from STE to Ce. However, in terms of the fitting of the scintillation pulse shape, we argue that the decay time, which arises only from $5d\rightarrow 4f$ cerium emission and is insensitive to temperature [37], should be fixed as approximately 16 ns to fit the decay curves and then to discuss the model. Recently, the study of picosecond absorption spectroscopy by Li *et al.* [38] shows that Ce^{3+} in lanthanum bromide is apparently not a good electron or hole trapper. At least self-trapped holes in $LaBr_3$ appear to be better at capturing electrons than Ce^{3+} ions are at capturing holes. The energy transport from host to activator is responsible for the scintillation of $LaBr_3$:Ce^{3+} proceeds by STE creation within 1 ps and then energy transfer more than by the sequential trapping of holes and electrons on Ce^{3+} ions [38]. Detailed scintillation rise-time measurements in $LaBr_3$:Ce with fast coincidence methods by Glodo *et al.* [35] and Seifert *et al.* [31] have identified a fast stage and a slower stage of scintillation rise for $LaBr_3$:5%Ce given as 380 ps [35] or 270 ps [31], and 2.2 ns [35] or 2.0 ns [31], respectively. Furthermore, the approximately

300-ps process is further suggested by Li *et al.* [38] as the dipole-dipole transfer to Ce from STEs created in the close neighborhood, and the approximately 2.1-ns process is the thermally activated migration and energy transfer at room temperature in 5%Ce-doped $\mathrm{LaBr_3}$. For $\mathrm{LaBr_3}$:Ce with higher concentration, it is possible that Ce ions can be excited directly. For example, the extreme case with 100% Ce concentration, $\mathrm{CeBr_3}$ should be the direct excitation and radiative emission of $\mathrm{Ce^{3+}}$ ions. To conclude, the scintillation mechanism in $\mathrm{LaBr_3}$:Ce with lower concentration, for example less than 5%, at room temperature is mainly first the creation of host STEs, then the migration and/or energy transfer from STEs to $\mathrm{Ce^{3+}}$ ions and finally the radiation emission of excited $\mathrm{Ce^{3+*}}$ ions:

$$e + h + \mathrm{Ce}^{3+} \rightarrow \mathrm{STE} + \mathrm{Ce}^{3+} \rightarrow \mathrm{Ce}^{3+*} \rightarrow \mathrm{Ce}^{3+} + h\nu.$$

A model of excitation transport and interaction in a particle track is established to fully explore the scintillation mechanism of $\mathrm{LaBr_3}$:Ce, shown as Fig. 1. In detail, the model can be separated into two main stages. The first stage includes the hot and thermalized free charge-carrier diffusion, electric field transport, and the form of STEs. The second stage includes the migration and energy transfer from STEs to $\mathrm{Ce^{3+}}$ ions, second-order nonlinear quenching between STEs or between excited $\mathrm{Ce^{3+}}$ ions, and radiative recombination. In particular, apart from the direct excitation of $\mathrm{Ce^{3+}}$ ions, only STEs formed in the first stage can have access to the second stage and transfer their energy to Ce and account for scintillation.

B. Diffusion-limited rate and transport equations for local light yield and decay curve versus on-axis initial excitation densities in particle tracks

The diffusion-limited rate and transport equation illustrating the local light yield (LY) and scintillation decay curve for $\mathrm{LaBr_3}$:Ce in our model are calculated using Eqs. (1)–(5).

$$\frac{dn_e}{dt} = G_e + D_e\nabla^2 n_e + \mu_e \nabla \cdot n_e \vec{E} - K_{1e}n_e - Bn_e n_h - K_3 n_e n_h n_e - K_3 n_e n_h n_h, \tag{1}$$

$$\frac{dn_h}{dt} = G_h + D_h\nabla^2 n_h + \mu_h \nabla \cdot n_h \vec{E} - K_{1h}n_h - Bn_e n_h - K_3 n_e n_h n_e - K_3 n_e n_h n_h, \tag{2}$$

$$\frac{dN_{\mathrm{STE}}}{dt} = G_{\mathrm{STE}} + D_{\mathrm{STE}}\nabla^2 N_{\mathrm{STE}} - (R_{\mathrm{STE}} + Q_{\mathrm{STE}} + S_T)N_{\mathrm{STE}} + Bn_e n_h - K_{2E}(t)N_{\mathrm{STE}}^2, \tag{3}$$

$$\frac{dN_{\mathrm{Ce^*}}}{dt} = G_{\mathrm{Ce^*}} + S_T N_{\mathrm{STE}} - R_{\mathrm{Ce^*}}N_{\mathrm{Ce^*}} - K_{2\mathrm{Ce^*}}(t)N_{\mathrm{Ce^*}}^2, \tag{4}$$

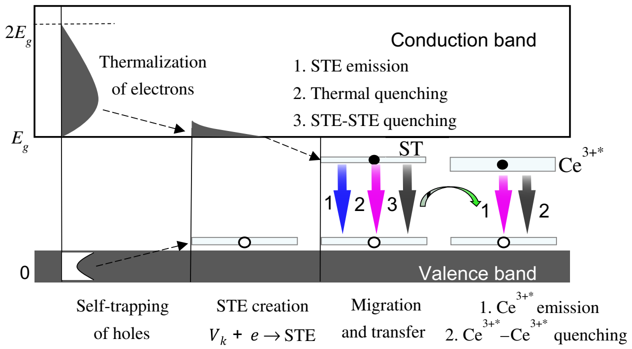

FIG. 1. Illustration of scintillation processes of physical mechanism in $\mathrm{LaBr_3}$:$\mathrm{Ce^{3+}}$ crystals, including the conversion of free electrons and hole, the thermalization of hot electrons and instant self-trapping of holes, the charge-carrier diffusion and the formation of STE, the migration and energy transfer from STE to Ce ions, and finally luminescence of excited $\mathrm{Ce^{3+}}$* ions.

$$S_T = S_T^0 \cdot \frac{n_{\mathrm{Ce}}^0 - N_{\mathrm{Ce^*}}}{n_{\mathrm{Ce}}^0}. \tag{5}$$

Equations (1) and (2) describe the first stage of free electrons and holes. The first stage also consists of two processes. The hot charge carriers, especially hot electrons, first diffuse outward and get thermalized. After thermalization, the distinct hot diffusion of electrons and holes creates an inner electric filed. Out-diffused electrons is then driven back to form STEs. Equations (3)–(5) describe the second stage of STEs and $\mathrm{Ce^{3+}}$ ions. We now describe each of the terms in these equations from the view of scintillation processes and their significant influences on the light yield and scintillation time profiles.

During the thermalization process of the first stage, which lasts for several picoseconds, the electrons and holes are excited with high excitation density and therefore diffuse outward and lose their excess kinetic energy (approximately eV) by impacting with the crystal lattice. Meanwhile, the outward free electrons and holes may suffer from linear trapping of defects or the third Auger quenching process, which may have a significant effect on the light yield of the scintillators and is ionization density dependent. During the thermalization, part of the free electrons and holes pair together and form STEs within several picoseconds, known as instant STEs, while the others remain free. For simplification, the formation process of STEs within the thermalization process, which is approximately 1 ps for $\mathrm{LaBr_3}$ [10,31,38], is regarded as the instant generation term.

The first terms of Eqs. (1)–(4), $G_{e,h}$, G_{STE}, and $G_{\mathrm{Ce^*}}$, are, respectively, the generation terms of free electrons and holes, instant STEs, and directly excited $\mathrm{Ce^{3+}}$ ions immediately after thermalization. Generally, a cylindrical Gaussian radial profile with a track radius of $r_0(\sim 3\ \mathrm{nm})$ is adopted to describe the distributions of excitations (including electrons, holes, excitons, and excited dopant ions) as reviewed in Ref. [33]. The radial distribution and its magnitude, the on-axis excitation density n_0, is shown as follows:

$$n(r, t = 0) = n_0 exp(-r^2/r_0^2), \tag{6}$$

$$n_0 = \frac{dE/dx}{\pi r_0^2 \beta E_{\mathrm{gap}}}, \tag{7}$$

where dE/dx is the energy-dependent linear energy transfer of a particle (electron/α). βE_{gap} is the average energy invested per electron hole pair. r_0 is the initial track radius, which is determined by the diffusion of hot holes during the thermalization process. In particular, the ionization densities produced on the end of an electron track can be as high as approximately 10^{20} cm^{-3} and range out in a very short distance.

The second terms $D_{e,h}$ and D_{STE} of Eqs. (1)–(3) denote the diffusion of free electrons and holes and STEs. As described in Ref. [13], holes in alkali halides are self-trapped very quickly, which is 50 fs for NaI from quantum molecular-dynamics calculations. Due to such rapid self-trapping, the hole Eq. (2) is simply written in terms of the density of the self-trapped holes (STHs), n_h, diffusing with the hopping diffusion coefficient of the self-trapped holes. However, the thermalization of electrons is somewhat complicated, and the cooling of the hot electrons in $\mathrm{LaBr_3}$:Ce is rather slow due to its low longitudinal optical phonon frequency (ω_{LO}) [10]. A mean thermalization time of 1 ps is characterized for $\mathrm{LaBr_3}$ due to its very similar ω_{LO} to NaI crystal [10,39], of which the mean thermalization time calculated by Wang *et al.* [40] is approximately 1 ps using the NWEGRIM Monte Carlo code at PNNL [40]. The longitudinal optical phonon frequency is 3.6×10^{13} s^{-1} and 3.47×10^{13} s^{-1} for $\mathrm{LaBr_3}$ and NaI, respectively. The thermalization time is further supported by the picosecond-absorption-spectroscopy experiment to be less than 1 ps under two-photon excitation of the host producing carriers near the band edges [38]. According to Wang *et al.* [40], hot electrons run outward to a radial peak of approximately 30 nm for fluorides ($\mathrm{CaF_2}$ and $\mathrm{BaF_2}$) and 50 nm for iodides (NaI and CsI), with a tail extending as far as 100 to 200 nm. Since D_e is a function of the electron temperature T_e, it is difficult to precisely model the hot diffusion process. A similar step-wise time-dependent electron diffusion coefficient proposed by Lu *et al.* [13,14] is adopted such that $D_e(t < \tau_{\mathrm{hot}})$ has a constant value to reproduce the distribution of electrons with peaks r_{hot} at several tens of nanometers. However, based on first-principles calculations [18,39] and the "decision tree" of inorganic scintillators proposed by Li *et al.* [32], $\mathrm{LaBr_3}$:Ce, unlike alkali halide, is a multivalent compound with a dense and flat set of $4f$ conduction bands approximately 3.5 eV above the conduction-band minimum (CBM) and thus smaller electron group velocities for a smaller electron distribution range. The fourth terms, K_{1e} and K_{1h}, of Eqs. (1) and (2) are the trapping from deep traps or defects of the crystal. The sixth and seventh terms, K_3, of Eqs. (1) and (2) are the third-order Auger recombination rates of free carriers. Since the hot diffusion term of free electrons greatly reduces the ionization density, the Auger quenching process in $\mathrm{LaBr_3}$:Ce is trivial based on the parameters measured by a laser Z scan of similar materials, which is discussed in Sec. II C.

After thermalization, the excitations diffuse with the thermalized diffusion rate, which is described by the Einstein equation, $D = \mu kT$. In particular, the diffusion rate of electrons after thermalization is calculated by $D_e(t > \tau_{\mathrm{hot}}) = \mu_e kT$. Due to the significant differences in the diffusion rates of hot electrons and self-trapped holes (STHs or V_k center), a distinct spatial distribution of the electrons and holes creates an electric field. The migration of the free thermalized electrons and holes proceed due to the electrostatic forces. The direction of the electron current reverses from outward to inward as the thermalized conduction electrons are collected back toward the line charge STHs where recombination can occur. The third terms, μ_e and μ_h, of Eqs. (1) and (2) represent the electric field driven currents. The fourth term, $Bn_e n_h$, in Eqs. (1) and (2) is the bimolecular exciton formation characterized by rate constant B and proportional to the product of the electron and hole densities at a given location and time. The exciton formation term, $-Bn_e n_h$, is a loss term in Eqs. (1) and (2) but the extra source term in Eq. (3)'s exciton density of the STEs apart from the initial creation of the instant STEs during the thermalization process of the first stage.

As illustrated before, the processes of the sequential capture of free electrons or holes by dopant ions are almost absent, since Ce^{3+} is not a good trapper for both electrons and holes in $\mathrm{LaBr_3}$:Ce. The main part of the transport process is the migration and energy transfer from the STEs to the Ce^{3+} centers. In the third term of Eq. (3), R_{STE} and Q_{STE} are the rates of the radiative decay and thermal quenching of the STEs. S_T is the energy transfer rate of the STEs to Ce^{3+}. Since the energy transfer rate is proportional to the density of the unexcited Ce^{3+} ions, Eq. (5) denoting such a relationship is also introduced. Compared with the model proposed by Bizarri and Dorenbos [36], a second-order dipole-dipole quenching process, $K_{2E}(t)$, between the excited STEs is introduced, which plays a role in situations of high excitation densities and accounts for a lower light yield and possibly different decay curves. Dipole-dipole annihilation is a case of Förster transfer from one excited dipole to another excited dipole rather than to a ground-state dipole, resulting in the annihilation of the first dipole and possibly ionization of the doubly excited second dipole. The second-order rate constant can be expressed for immobile species as

$$K_2(t) = \frac{2}{3}\pi^{3/2}R_{dd}^3(t\tau_R)^{-1/2}, \tag{8}$$

where τ_R is the radiative lifetime of the excited state and R_{dd} is the Förster transfer radius depending on the overlap of the emission and absorption bands.

The first term, G_{Ce^*}, of Eq. (4) is the direct creation of the excited Ce^{3+} states. Only electrons with enough excess kinetic energy to excite the Ce^{3+} ions can create such initial excited Ce^{3+} states, which is especially significant for crystals with high dopant concentrations. The second term, $S_T N_{STE}$, of Eq. (4) is the main source of the excited Ce^{3+*} states from the energy transfer of the STEs. The third term, $-R_{Ce^*}N_{Ce^*}$, of Eq. (4) is the radiative recombination of the excited Ce^{3+*} states and is the dominant source of luminescence. In particular, the second dipole-dipole quenching between excited Ce^{3+*} ions, $K_{2Ce^*}(t)$, is proposed and verified to account for the nonproportionality and pulse-shape difference for high excitations, which is discussed later in Sec. II C.

C. The material input parameters

This section details the parameters, listed in Table I, used in our model. Most of the parameters are found directly in the literature when possible, or scaled by quantitative physical arguments from parameters known in similar materials.

The initial Gaussian ionization radius of the track, r_0, is normally considered as 3 nm, which is evaluated by Z scan [10] and kinetic Monto Carlo simulations in NaI and CsI [16,18,40]. $LaBr_3$ is also a heavier halide and the holes are self-trapped [46] as in the case of NaI and CsI according to the simulation, thus the same parameter $r_0 = 3$ nm is used for $LaBr_3$.

The value of $\beta E_{gap} = 13$ eV, average energy invested per electron-hole pair, is adopted from the best-known light yield, 77 000 photons/MeV, of $LaBr_3$:Ce, Sr. The codoping of 100 ppm Sr enhances the shallow trapping of the free electrons from the capture of the defects and thus increases the light yield. Such small codoped Sr should not change the number of ionized electron-hole pairs, which is determined by the host $LaBr_3$ and heavy-dopant Ce ions. β is calculated as 2.2 based on the band gap of 5.9 eV. $LaBr_3$ is an outstanding inorganic scintillator with high light yield, a value of 2.2 is reasonable compared with a value of 2.5 in most materials.

The thermalized electron mobility μ_e in $LaBr_3$:Ce is dependent on the dopant Ce concentration and can be calculated based on the ionized impurity scattering [41]. The thermalized conduction electron diffusion coefficient D_e is given in terms of μ_e by the Einstein relation, $D = \mu kT/e$.

TABLE I. Parameters (and their literature references or comments on methods) used for the calculation of the light yield, proportionality, and scintillation time profile of $LaBr_3$:Ce at 295 K.

Parameter	Value	Units	Refs. and notes
r_0	3	nm	Refs. [10,40] for NaI, Ref. [13] for CsI
βE_{gap}	13(β = 2.2)	$(eV/e - h)_{avg}$	$\eta = 77\,000$ ph/MeV for $LaBr_3$:Ce, Sr [5]
ε_0	10	N/A	Ref. [39,41]
$\eta_{e,h}$	0.18	N/A	Payne-Onsager model, Ref. [11]
μ_e	2	$cm^2\ V^{-1}\ s$	Ref. [41]
$D_e(t > t_{hot})$	5.1×10^{-2}	$cm^2\ s^{-1}$	$D_e = \mu_e kT/e$
τ_{hot}	1	ps	Ref. [10,41] for NaI (with same ω_{LO})
μ_h	1×10^{-4}	$cm^2\ V^{-1}\ s$	Ref. [13] for CsI
D_h	2.6×10^{-6}	$cm^2\ s^{-1}$	$D_h = \mu_h kT/e$
$B(t > \tau_{hot})$	2.5×10^{-7}	$cm^3\ s^{-1}$	Ref. [13,38]
K_3	4.5×10^{-29}	$cm^6\ s^{-1}$	Ref. [13] for CsI, not sensitive
K_{1e}	1×10^8	s^{-1}	Ref. [13]
K_{1h}	0	s^{-1}	Ref. [13,42]
r_{hot}	25	Nm	$LaBr_3$:5%Ce nPR curve, smaller than 50 nm. Ref. [43]
$D_e(t < t_{hot})$	3.1	$cm^2\ s^{-1}$	to reproducerr_{hot}at τ_{hot}
R_{STE}	1×10^6	s^{-1}	1 us decay time of STE at 80 K, Ref. [42]
Q_{STE}	0	s^{-1}	negligible at room temperature. Ref. [36]
S_{fast}	$1/(0.27 \times 10^{-9})$	s^{-1}	Ref. [31]
S_{slow}	$1/(2.0 \times 10^{-9})$	s^{-1}	Ref. [31]
A_{fast}	0.72	N/A	Ref. [31]
R_{Ce}	$1/(15.4 \times 10^{-9})$	s^{-1}	Ref. [31]
D_{STE}	2.6×10^{-6}	$cm^2\ s^{-1}$	$D_{STE} \approx D_{STH}$, Ref. [44]
K_{2Ce^*}	9.7×10^{-17}	$t^{-1/2}\ cm^3\ s^{-1/2}$	Calculated from quenching factor of α particles with $CeBr_3$, Ref. [45]
K_{2E}	5.1×10^{-17}	$t^{-1/2}\ cm^3\ s^{-1/2}$	Calculated from quenching factor of α particles with $LaBr_3$:Ce, Ref. [45]

The mobility of self-trapped holes can be estimated from their thermal hopping rate [40,47]. Since there are no direct measurements of this rate in $LaBr_3$, the parameter from CsI crystal is taken as a reference since they are all heavier halides. Moreover, the mobility of self-trapped holes is very small, which is not a sensitive parameter in the model, and can be even set to 0 as an approximation. The diffusion coefficient of STE, which can be calculated with the Einstein relation, is considered the same as STH in our model, since recent electronic structure calculations have provided evidence that they are equally mobile in NaI [48,49].

The thermalization process is hypothesized, which greatly affects the nonproportionality of the γ or electron response [13,32]. The fraction of free carriers, $\eta_{e,h}$, and the thermalization distance, r_{hot}, are the two significant parameters that affect the nonproportionality. Williams and coworkers hypothesize that extensive charge separation, during the thermalization process, combined with the following electrostatic attraction is the root cause for nonproportionality at high incident energies [13,32]. Later on, Prange *et al.* [18] simulated the electron thermalization of six scintillating crystals using the microscopic kinetic Monte Carlo model and further supported the hypothesis proposed by Williams. They proposed that the thermalization distances are positively correlated with measured nonproportionality. Whereas, the model proposed by Payne *et al.* [2,11,50] also showed that the fraction of the excitations that are free carriers significantly influences the nonproportionality. The Payne-Onsager model is based on theories by Onsager, Birks, Bethe-Bloch, Landau and by the appropriate choice of parameters and can reproduce the experimental data well [2,11]. For a given dE/dx, the Birks and Onsager mechanisms are the two main processes that compete with each other. Actually, the Onsager mechanism arises from Coulombic attraction of carriers, which is similar to the process of charge separation proposed by Williams. Based on the fitted parameters of the Payne-Onsager model, $\eta_{e,h}$ is one of the key parameters to cluster the scintillators. Alkali halides tend to possess a high fraction of free carriers and show more "hump" size in electron- and γ-response curves. The fitted $\eta_{e,h}$ parameters with the Payne-Onsager model are also in good accordance with the kinetic Monto Carlo simulation results of Wang *et al.* in CsI(Tl) and NaI(Tl) crystals [40]. Wang *et al.* also calculated that the radial peak of thermalization distance is approximately 30 nm for fluorides (CaF_2 and BaF_2) and 50 nm for iodides (NaI and CsI). Further calculation from Prange *et al.* [18] showed that the thermalization distance (r_{hot}) is larger and the fraction of free carriers ($\eta_{e,h}$) is smaller compared with the results of Wang *et al.* Both kinetic Monte Carlo simulation shows a sophisticated behavior that $\eta_{e,h}$ varies with the incident γ-ray energy. Because lower incident energy means a higher ionization density and thus stronger electrostatic filed and higher percentage of electron-hole pairs that recombine during electron thermalization. Moreover, not only the thermalization time, but also the thermalization distance is dependent on the group velocity of hot electrons. Calculations show that monovalent and simple alkali halides (NaI and CsI) tend to have a longer thermalization distance than multivalent and complex systems (YAP, SrI2, and BaBrI/Cl). For simplicity, the fraction of free carriers is considered as a constant and the fitted value $\eta_{e,h} = 18\%$ from the Payne-Onsager model for $LaBr_3$:5%Ce is taken as a reference. A step-wise time-dependent electron diffusion coefficient such as that proposed by Lu *et al.* is adopted as well, so that $D_e(t<\tau_{\mathrm{hot}})$ has a constant value that reproduces the result of r_{hot}(peak) (<50 nm) in the solution of Eq. (1) at the end of $\tau_{\mathrm{hot}} \approx 1$ ps. Pairs of ($\eta_{e,h}$, r_{hot}), with $\eta_{e,h}$ from 0.1 to 0.2 to 0.5 and r_{hot} from 10 to 25 nm to 50 nm, are simulated and compared with the experimental data, shown in Fig. 2. With this small $\eta_{e,h} = 18\%$, the nonproportionality curve is not sensitive to the thermalization distance, since most free carriers have combined each during the thermalization process. A value of 25 nm, smaller than the 50 nm for CsI, is chosen for the multivalent $LaBr_3$. To conclude, higher $\eta_{e,h}$ and r_{hot} show more "halide hump," which is in accordance with previous researches. $LaBr_3$:Ce belongs to multivalent and possesses a flat electron response and very small "halide hump."

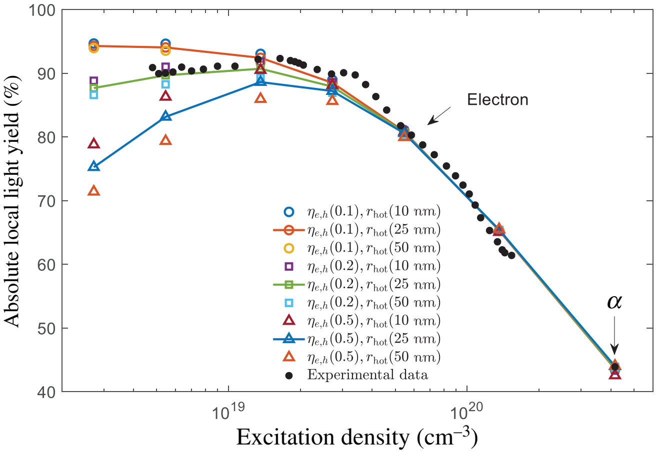

FIG. 2. Simulations of the absolute local light yield with excitation density under different thermalization parameters, along with the measured experimental data.

The mean thermalization time $\tau_{\mathrm{hot}} \approx 1$ ps, due to its very similar ω_{LO} with NaI crystal, is further confirmed by the picosecond-absorption-spectroscopy experiment to be less than 1 ps under two-photon excitation of the host producing carriers near the band edges.

K_{1e} and K_{1h} are the electron and hole trapping rate of deep defects. The capture of deep defects is the cause of afterglow, and thus a large $K_{1e} = 2.7 \times 10^{10}\ \mathrm{s}^{-1}$ is fitted in the CsI crystal. Whereas K_{1h} is negligible compared with K_{1e} due to the much smaller velocity approaching the trap in alkali halide [13]. However, the residual intensity induced by the x-ray exposure of $LaBr_3$:Ce is measured to be less than 0.01% after 200 s [42]. First-principles calculation from Aberg *et al*. shows that in the ground state of $LaBr_3$:Ce, Ce preferentially substitutes for La with small distortions and adopts a neutral charge state corresponding to a Ce^{3+}-$4f^15d^0$ configuration. The intrinsic defects of pure $LaBr_3$ is several orders smaller than $LaBr_3$ doped with 200 ppm Sr, which gives rise to a shallow acceptor substituting on a lanthanum site and thus improves the linearity of the photon light yield with respect to the energy of incident electron or photon. Moreover, the efficiency of light emission for $LaBr_3$:Ce is sufficiently high, so that free carriers are merely trapped by deep defects. A very small number of $K_{1e} = 1 \times 10^8$ s^{-1}, not much difference to the value $K_{1e} = 0$ s^{-1}, is used to kill the out-diffused and stopped free electrons and is not driven back to form STE with STH for low ionization density. We also estimate the influence of K_{1e} by changing its value from $0 \sim 1 \times 10^{10}$ s^{-1}, the light yield of low excitation density changes less than 6%, while it has little influence on the high excitation density due to the competition process of recombination. K_{1h} is neglected as 0, due to the small intrinsic deep defect and much lower velocity compared with the electron.

K_3 is the third-order Auger recombination rate of free carriers. We evaluate K_3 from 0 to 6.6×10^{-29} cm^{6}s^{-1} and nothing changes. We find that K_3 does not affect the nonlinear quenching, since the hot diffusion of free electrons rapidly reduces the ionization density.

The energy transfer rate S_T, from STEs to Ce^{3+} ions, and the decay rate $R_{Ce^{3+}*}$ of the excited Ce^{3+*} can be measured precisely from the decay time profile of the γ rays with the TCSPC method. The thermalization process, which lasts several picoseconds, rarely influences the decay profile with the time scale of nanoseconds. Moreover, the higher-order quenching terms can also be neglected for low-ionization density γ rays, and thus does not influence the decay profiles. Detailed scintillation rise-time measurements in $LaBr_3$:Ce with fast coincidence methods by Glodo *et al.* [35] and Seifert *et al.* [31] identify a fast stage (S_{fast}) and a slower stage (S_{slow}) of scintillation rise reported as approximately 300 ps and 2.1 ns, respectively. The percentage of the fast process (A_{fast}) is approximately 72%. The 300-ps process is further suggested by Li *et al.* [38] as the dipole-dipole transfer to Ce from STEs created in the neighborhood, and the 2.1-ns process is the thermally activated migration and energy transfer at room temperature in 5%Ce-doped $LaBr_3$.

The dipole-dipole quenching parameters of K_{2Ce*} and K_{2E}, mainly decrease the light yield for particles with high ionization densities, are calculated from the α/β ratio of internal radioactive α particles of $CeBr_3$ and $LaBr_3$:5%, respectively.

The conservation and thermalization stage normally takes place in the first several picoseconds, during which the nonlinear quenching is already completed or predetermined. For halides, the competition between the outrun of hot electrons, thus captured by defects, and the formation of STEs within the inner static electric field strongly influence the quantity of carriers effective for further evolution. For α particles, of which the linear energy transfer (LET) is higher than 300 MeV cm^2 g^{-1}, the independent fraction of free electrons and holes is near zero and STEs are formed effectively under a strong electrostatic force [51]. The model for α particles can be simplified as the one proposed by Bizarri and Dorenbos [36] but with the dipole-dipole quenching terms added for high ionization, in which STEs are formed instantly:

$$\frac{dN_{STE}}{dt} = G_{STE} - (R_{STE} + Q_{STE} + S_T)N_{STE} - K_{2E}(t)N_{STE}^2, \tag{9}$$

$$\frac{dN_{Ce*}}{dt} = S_T N_{STE} - R_{Ce*}N_{Ce*} - K_{2Ce*}(t)N_{Ce*}^2, \tag{10}$$

$$S_T = S_T^0 \cdot \frac{n_{Ce}^0 - N_{Ce*}}{n_{Ce}^0}. \tag{11}$$

The energy transfer rate of STEs and the decay rate of excited Ce^{3+} ions have already been measured with γ excitation and previously discussed. What remains unknown are the two second-order rate constants for the quenching terms of the STEs and the excited Ce^{3+} ions. Fortunately, the second-order rate constants K_{2Ce*} can be calculated using $CeBr_3$ crystals. The very fast transport process, 165-ps rise time $t_{10\%-90\%}$ for x-ray excitation, from free electrons and holes to the Ce^{3+} ions is neglected, which may have limited variation of the calculated parameter K_{2Ce*}. The excitation of $CeBr_3$ can be considered as the direct excitation of Ce^{3+} ions and the kinetic equation for $CeBr_3$ is then

$$\frac{dN_{Ce*}}{dt} = G_{Ce*} - R_{Ce*}N_{Ce*} - K_{2Ce*}(t)N_{Ce*}^2. \tag{12}$$

The generation term G_{Ce*} can be calculated using Eq. (6) with βE_{gap}=16.7 eV calculated from the light yield of 60 000 Ph/MeV. The decay rate is the inverse of the measured decay time 17 ns. Using the local light yield for the α particles, the calculated K_{2Ce*} is 0.097×10^{-15} cm^3 s$^{-1/2}$. After the determination of K_{2Ce*}, the second-order rate constants K_{2E} can be similarly ascertained using the local light yield for the α particles in $LaBr_3$:Ce by solving Eqs. (9)–(11). The calculated K_{2E} is then 0.051×10^{-15} cm^3 s$^{-1/2}$.

III. PROPORTIONALITY AND ITS IONIZATION DENSITY DEPENDENCE

A. Experimental data

The intrinsic response of a scintillator is usually not proportional to the incident particle energy, which is normally considered caused by the nonlinear quenching of high ionization density as the electrons slow along the track. The light yield produced by internally generated electrons over a wide range of energies can be measured by the Compton coincidence [7,8,52,53] and Kdip [9,54] methods. Figure 3(a). shows the measured electron responses of the $LaBr_3$:5%Ce^{3+} crystal using the SLYNCI [46] and Kdip [33] methods at room temperature.

The initial ionization density values vary from cell to cell along the length of the track with the variation in dE/dx and we calculate the local light yield for each local dE/dx value. The Penelope model from the Geant4 simulation is chosen to describe the variation in dE/dx with the electron energy. Although the modified Bethe equation is used by many previous researches [2,11,55–57], the Penelope model, shown in Fig. 3(b), can more properly describe the scintillation response of low-energy electrons, which tends to be constant between 0.1 and 0.4 keV.

Unlike the clustered track of CsI [13], the track of $LaBr_3$ is linear [58] so the intermediate local light yield can be calculated from experimental data. For an electron with an initial energy E_0, the measured light yield, $\eta(E_0)$, is the average of the integration of the local light yield along the electron track. We then calculate the local light yield, $dL/dE(\varepsilon)$, for one cell with electron energy ε using the following equations:

$$\eta(E_0) = \int_0^{E_0} \frac{dL}{dE}(\varepsilon) d\varepsilon / E_0, \tag{13}$$

$$\frac{dL}{dE}(\varepsilon) = \frac{d[\varepsilon \cdot \eta(\varepsilon)]}{d\varepsilon}. \tag{14}$$

Similarly, the quenching of the αa particles, which causes the nonlinear quenching in the high-density part of the ionization tracks, is also discussed [55]. The α/β ratio (or quenching factor) of the α particle and the corresponding calculated local light yield in the $LaBr_3$:Ce^{3+} detector are shown in Table II. Assuming an α particle with an initial energy of 7386.1 keV and decreasing its energy to 6819.2 keV, the stopping power from the ASTAR databases [55] of the particle changes little and can be considered a constant and represented by the mean values 301 MeV cm^2 g^{-1}. The mean local light yield, dL/dE, for an α particle with dE/dx of 1514 MeV cm^{-1} (= 301 MeV cm^2 g^{-1} × 5.03 g cm^{-3}) is 0.483.

To conclude, the relationship between the local light yield and dE/dx for both the electron and α particles are shown in Fig. 4. They can be used to compare our model directly with the change from dE/dx to the excitation density with Eq. (6).

B. Model results

Figure 4 shows the calculated normalized local light yield (normalized with excitation density of 2.7×10^{18} cm^{-3}, corresponding to the LET of 10 MeV cm^{-1})

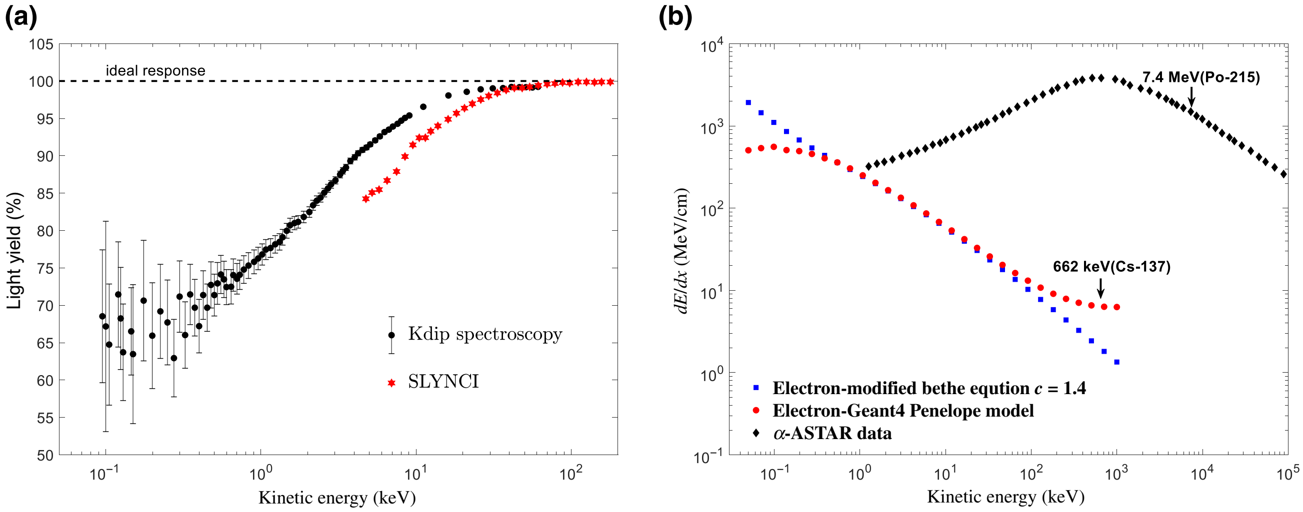

FIG. 3. (a) Combined plot of the two experiments for $LaBr_3$:5%Ce^{3+} (300 K). The kinetic energy (keV) axis represents the electron energy. The light-yield (%) axis represents the normalized light yield. The black dotted points are measured with the Kdip method and are available in Ref/ [33], while the red hexagonal points are measured with the Compton coincidence method and are available in Ref. [46]. (b) dE/dx of the electrons with electron energy in $LaBr_3$:Ce.

TABLE II. The α/β ratio measured in different materials using time-amplitude analysis to separate the Po-215 and Rn-219 α peaks from the α internal background [45] and the calculated mean dL/dE of α particles with energy from 7386.1 to 6819.2 keV. The density [5] of LaBr$_3$:Ce is 5.03 g cm^{-3} and CeBr$_3$ is 5.18 g cm^{-3}, which is used to convert the stopping power of the materials to dE/dx.

Material	Isotope	True α energy (keV)	α/β ratio	Initial stopping power (MeV cm^2 g^{-1})	Mean dE/dx (MeV cm^{-1})	Mean dL/dE
LaBr$_3$:5%Ce	Po-215	7386.1	0.363	294	1514	0.483
LaBr$_3$:5%Ce	Rn-219	6819.2	0.353	308		
CeBr$_3$	Po-215	7386.1	0.266	294	1559	0.374
CeBr$_3$	Rn-219	6819.2	0.257	308		

with the on-axis excitation density using the parameters of Table I in Eqs. (1)–(5) for LaBr$_3$:5%Ce at room temperature. The red dots of our model fit the local light yield of both the electron and α particles very well. The simulated absolute light yield of 69.3 photons/keV for the low excitation density of the high-energy γ rays is approximately 90% of the ideal light yield, which corresponds to the measured light yield of 70 photons/keV. The ideal light yield of 77 photons/keV for LaBr$_3$:Ce is assumed as the best-known value of LaBr$_3$:Ce, Sr. The increase in the light yield for the co-doped LaBr$_3$:Ce, Sr is attributed to the efficient shallow trapper of the Sr defects and reduced the loss of the free electrons and holes by diffusing outward and being captured by the defects [59].

Since LaBr$_3$:Ce has linear track, the measured light yield, $\eta(E_0)$, is the average of the integration of the local light yield along the electron tracks using Eq. (13). The comparison between integrated light yield of the model and the experimentally measured light yield of the electrons with the Kdip method is shown in Fig. 5, which shows good accordance for electrons with energy of 0.1–100 keV.

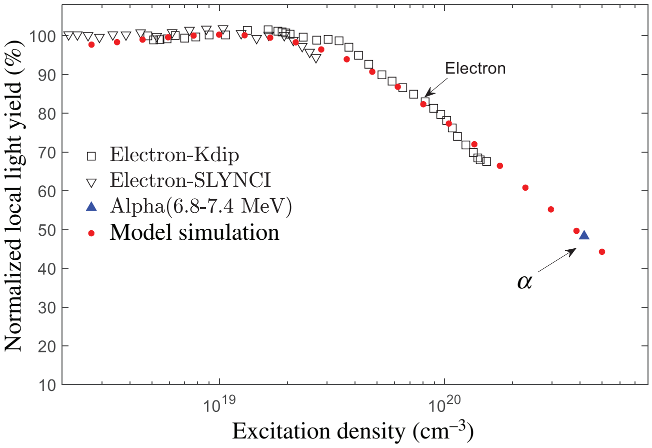

FIG. 4. Calculated normalized local light yield with the excitation density of LaBr$_3$:Ce from different experiments. The black open inverted triangles are the results measured with the SLYNCI method, the black open squares are the results measured with the Kdip method, the blue solid triangle is the data measured with 6.9–7.4 MeV α particles. The red dots are the simulation results of the model.

IV. PULSE SHAPE AND ITS IONIZATION DENSITY DEPENDENCE

The model includes the processes of linear energy transfer and radiative recombination, as well as nonlinear quenching, which influences the excitation-density-dependent pulse shapes. In this part, the decay curve of α and γ can be calculated with the model and is verified with experiments in the following sections.

A. Experimental setup and experimental data

A Ø10 × 5 - mm cylindrical LaBr$_3$:5%Ce^{3+} crystal is used. Since LaBr$_3$:Ce^{3+} is hygroscopic, the sample is packaged in a metal can with a quartz window to prevent long-term exposure to moisture. The scintillation time profiles under excitation of both α particles from intrinsic ^{227}Ac contamination and γ rays from a ^{22}Na source are measured using the delayed coincidence method [60], shown in Fig. 6.

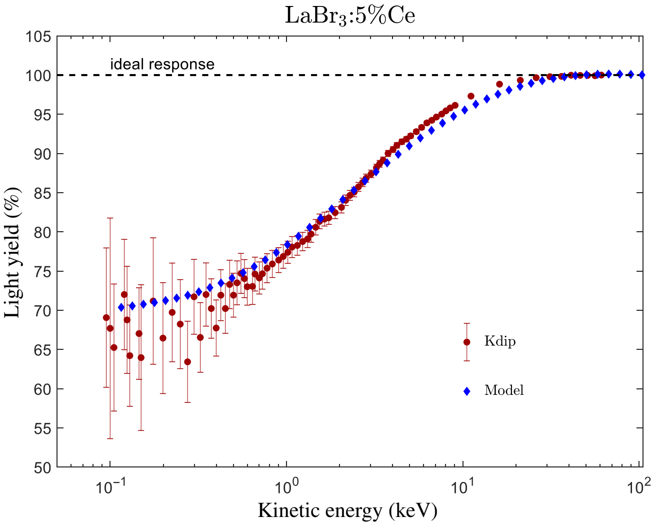

FIG. 5. Comparison between integrated light yield of the model and the measured light yield of the electrons.

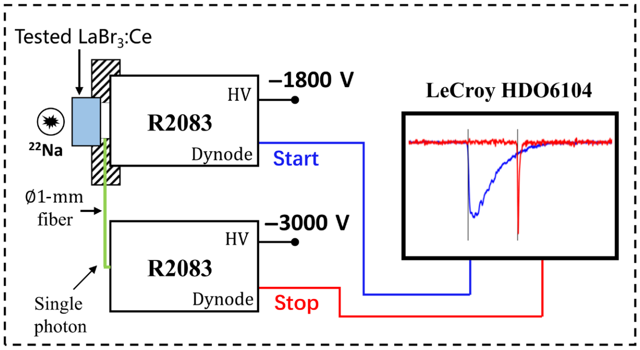

FIG. 6. Setup of time-correlated single-photon counting measurement.

Two R2083 PMTs are used as the start and stop detectors. A LeCroy HDO6104 oscilloscope (2.5 Gsps, 12 bit) is used to digitize the pulse shape of the start detector and a single photon signal of the stop detector to extract the time difference between the start and stop signal. The high-voltage (HV) supply of the start detector is 1800 V due to the saturation of the start detector, while the HV for the stop detector is 3000 V to achieve better timing resolution.

In our experiment, the start channel collected approximately one-third of the total light output. The peak-over-charge ratio (V_p/Q_{total}, which is the area normalized amplitude, also known as A/E) [23] with the charge are shown in Fig. 7(a). The PSD feature A/E is used to choose α events from an environmental γ background, which is similar to the charge comparison method (CCM) PSD feature used in our previous work [25]. The averaged pulse shapes, each with 2000 events, of the two colored rectangle regions are aligned by the 20% fraction of the peak amplitude and shown in Fig. 7(b). The averaged pulse shape of the α events is faster than the γ events both in the rising part and the decay part.

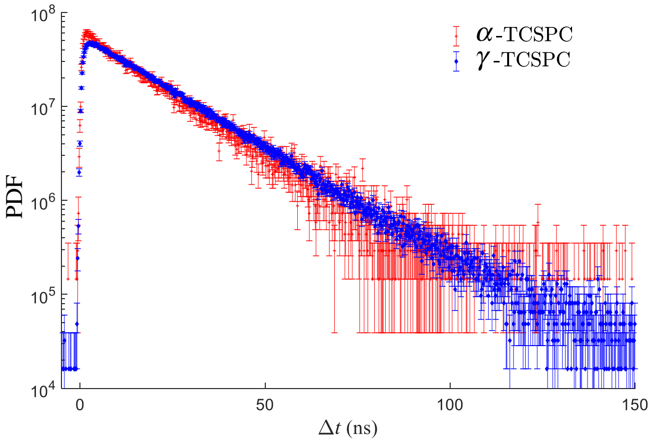

FIG. 8. Normalized time profiles of 511-keV γ rays and α particles in the LaBr$_3$:Ce^{3+} detector, measured with the TCSPC method.

The measured time profile of both the α and γ particles (using a ^{22}Na source) with the TCSPC method is shown in Fig. 8. Due to the relatively small volume (approximately 0.393 cm^3) of crystals and the low α background count rate (0.082 cps cm^{-3}), the 30-day experimental data and 34 382 effective α events (single photon signal) are collected for the TCSPC measurement.

B. System response of TCSPC experimental setup

Before the verification of the model, the *impulse response function* (IRF) of the measured time profiles, which mainly consists of two factors, need to be determined. First, the timing resolution of the start and stop detectors convolute approximately a Gaussian response.

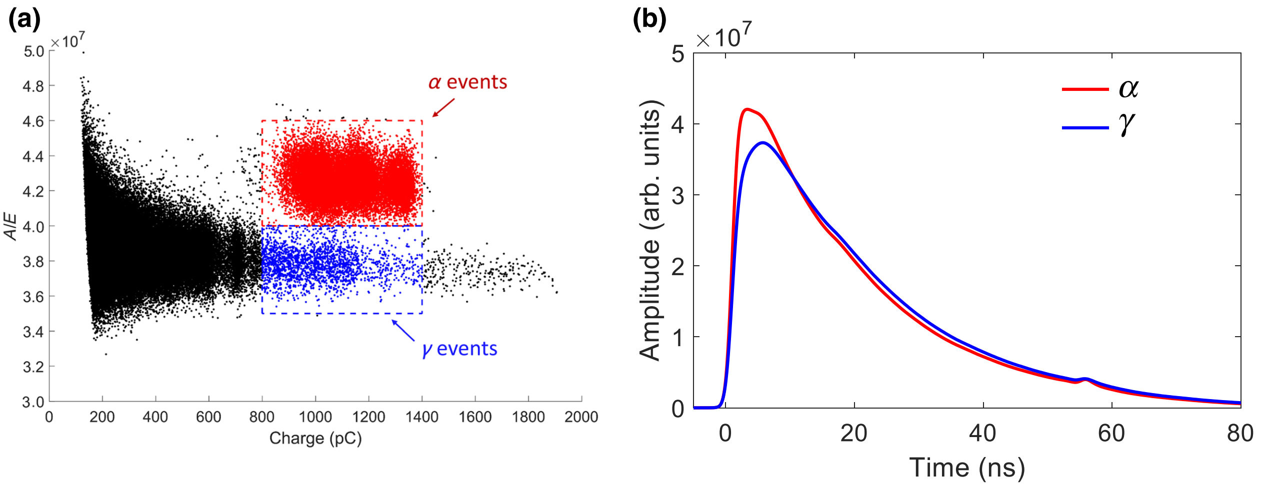

FIG. 7. (a) Distribution of the PSD feature A/E with energy. (b) Averaged pulse shapes of the events within the two colored rectangle regions.

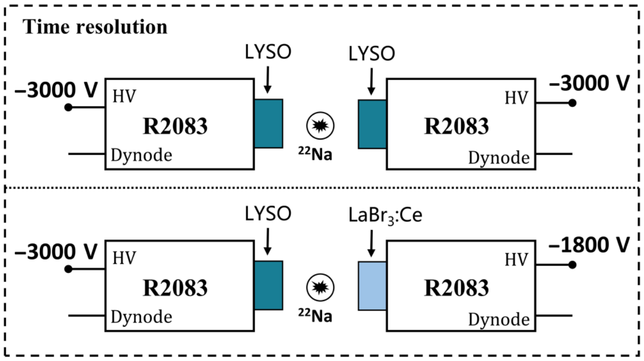

FIG. 9. Setup of calibration of TCPSC system time resolution.

Second, the photon transportation and bulk reabsorption following with the reemission due to the finite volume of the scintillation crystal also influence the scintillating time profiles characterized by the arrival times of collected photons.

1. Characterization of the timing resolution for TCSPC measurement

Two identical 5 × 5 × 5 mm lutetium yttrium oxyorthosilicate, $Lu_{2(1-x)}Y_{2x}SiO_5$:Ce (LYSO) crystals and a ^{22}Na source are used to calibrate the time resolution of the start detector ($LaBr_3:Ce^{3+}$), shown in Fig. 9.

The overall Gaussian IRF function of the system is then described by the convolution of the two Gaussian functions with a total FWHM of

$$\sqrt{(214\ \text{ps})^2 + (370\ \text{ps})^2} = 427\ \text{ps}.$$

2. Characterization of photon transportation and bulk reabsorption with Monto Carlo simulation

A Monto Carlo simulation of the photon collection of scintillator, including photon transportation and bulk reabsorption, based on Geant4 is carried out. For the simulation, photons are generated uniformly within the scintillator and collected by the optical coupling shown in Fig. 10(a). The parameters of the energy distribution, scattering length, and absorption length of the generated photons are taken from the experiment carried out by Herman *et al.* [61]. The re-emission of absorbed photons is not considered in the simulation. One million photons are generated uniformly and 85.3% of the photons are collected without absorption. The distribution of the photons' arrival times, which is not negligible with the mean transportation time of 372 ps compared with the fast rising component of 300 ps, is shown in Fig. 10(b).

A modified reabsorption model from the one in SrI_2:Eu [62] is used,

$$I(t) = \sum_i p_i I_i(t) = \frac{1}{\tau}\sum_i p_i \left(\frac{t}{\tau}\right)^{i-1} \frac{\exp(-t/\tau)}{(i-1)!}, \qquad (15)$$

where $I(t)$ is the intensity of the emission in time t and p_i is the probability of the collected photons with $(i-1)$ reabsorptions. However, Eq. (15) neglects the photon transportation response and only convolutes the time delay caused by the reabsorption. Multiple transportations caused by multiple reabsorptions are also considered in our model, which is especially not negligible for large crystals. The probability of the reabsorption of the ith remitted photon is considered the same, which is (1%–85.3%) in our case, and neglected

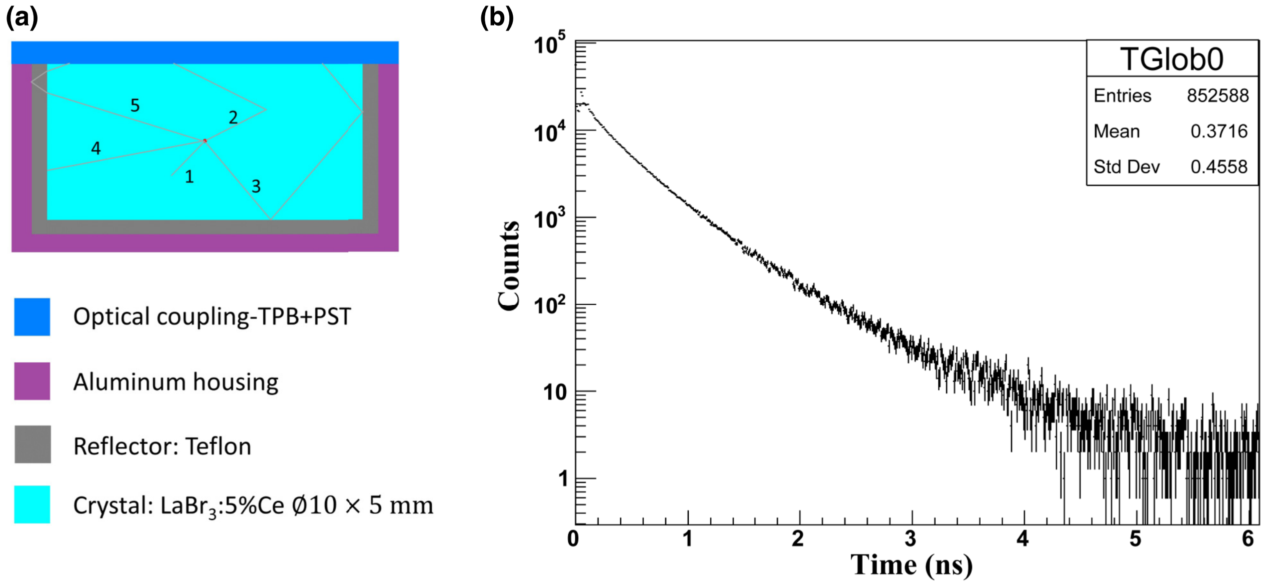

FIG. 10. (a) Illustration of the Monto Carlo simulation. (b) Distribution of the photons' arrival times within a Ø10×5-mm crystal.

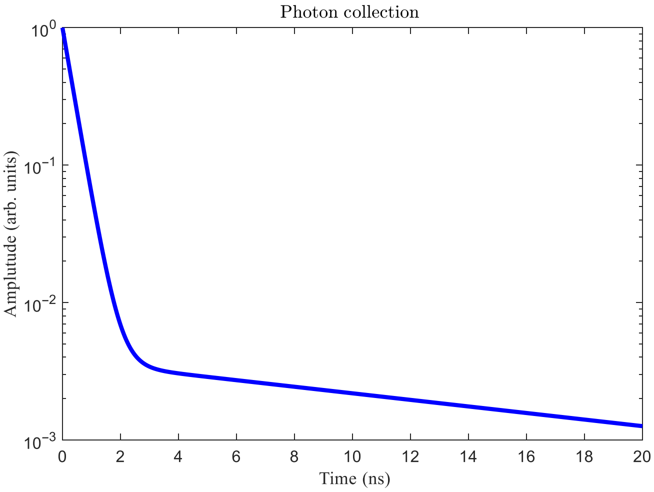

FIG. 11. Calculated response of photon collection, including multiple photon transportations and bulk reabsorptions.

the possible change caused by a small shift in the emission that reduces the overlap between the emission and absorption [63]. The calculated response of photon collection, named as PHC, of LaBr$_3$:5%Ce is shown in Fig. 11.

C. Model results

1. *Verification of γ pulse shape*

The experimental data and model calculation, which convolut the IRF of the system and the transportation and reabsorption of the crystal, are compared in Fig. 12. Superimposed is the original decay profile of the 511-keV γ rays fitted by Seifert *et al.* [31] on which the energy transfer rates from the STE to Ce^{3+} in our model are based. We test our model results with the experimental data using the χ^2/ndf statistic:

$$\chi^2/ndf = \frac{1}{N}\sum_{n=1}^{N}\frac{(M_n - E_n)^2}{E_n}, \tag{16}$$

where N is the total number bins and M_n is the measured number of entries in the nth histogram bin. E_n is the expected number of counts in the nth bin based on our model.

The calculated χ^2/ndf between the experimental data and our model is 1.223 for γ rays, which shows a good correspondence between our model and the experiment. It also suggests that the rate parameters describing the pulse shape of the γ rays in our LaBr$_3$:Ce^{3+} crystal is similar to those used in Ref. [31].

2. *Verification of α pulse shape*

With the determination of all of the parameters from the γ-ray pulse shape and the quenching of the α particles, the calculated time response of the α particles can be assessed, with a mean stopping power of 440 MeV cm^2 g^{-1} along the track. The comparison between the experimental data and model calculation after considering the system IRF and reabsorption is shown in Fig. 13(a), with $\chi^2/ndf = 1.011$, which demonstrates a good prediction of the scintillation time profile for α particles with high ionization density. The detailed rising part between the measured time profiles and the model results is shown in Fig. 13(b).

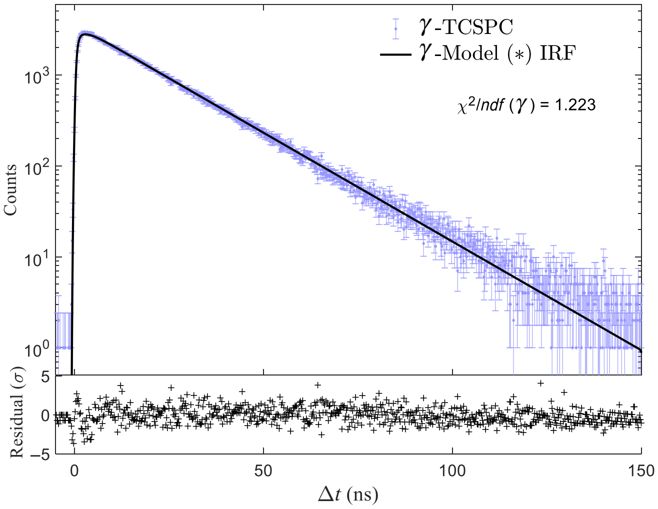

FIG. 12. The light blue is the measured decay profile of the 511-keV γ rays. The dotted black line is the model results with the convolution of the system IRF, photon transportation, and reabsorption. The red line is the original decay profile of the 511-keV γ rays fitted by Seifert *et al.* [31] measured with a small crystal.

A summary of α and γ pulse shapes from experiment and model calculation is shown in Fig. 14.

V. DISCUSSON OF THE GENERALITY OF THE MODEL

A. The α/β ratio with the Ce^{3+} concentration

According to research [55], the α/β ratio of LaBr$_3$:Ce^{3+} changes with the Ce concentration and shows a parabolic shape with a maximum at 5% Ce dopant. A better α/β ratio means less quenching and better nonproportionality and thus good energy resolution. Herein we discuss the underlying cause of this phenomenon. As discussed in our previous model, two quenching processes of both STEs and Ce^{3+*} can happen. Meanwhile, the rise time of the decay profile decreases with higher Ce concentrations due to the more efficient energy transfer process from STEs to Ce^{3+} ions.

For lower Ce concentrations, less than 5% Ce^{3+}, the lifetime of the STEs becomes longer. Therefore, the quenching between the STEs plays a leading role and decreases the α/β ratio. For Ce^{3+} concentrations higher than 5%, with a Ce^{3+} ion density 1.05×10^{20} cm^{-3}, the quenching

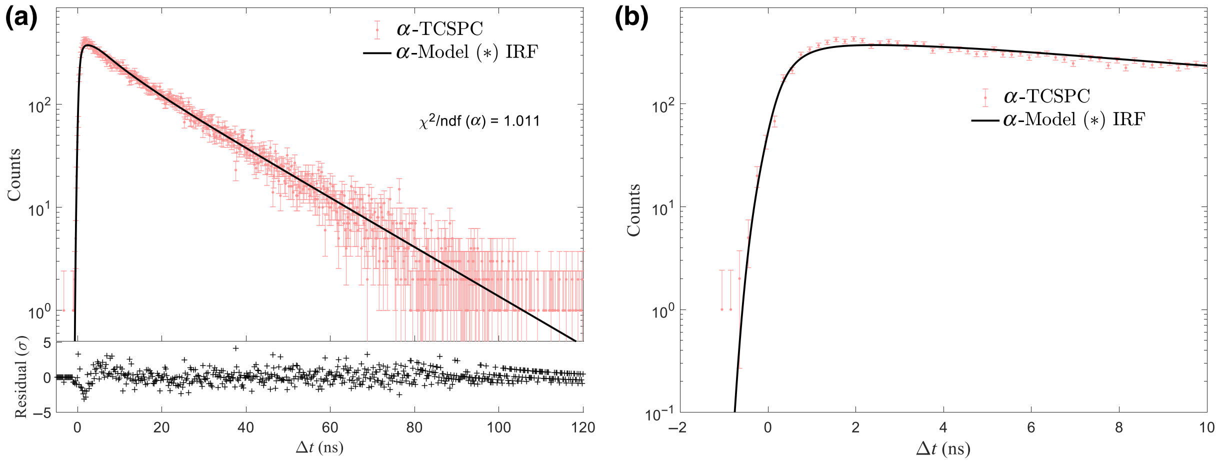

FIG. 13. (a). The light red data is the measured decay profile of the α particles. The dotted black line is the model results of the α particles with the convolution of the system IRF, photon transportation, and reabsorption. (b) Detailed comparison of the rising part between the model calculation and the experimental data.

between the excited Ce^{3+*} ions dominates and degrade the α/β ratio. The trade-off between these two quenching processes can qualitatively explain the shape of the α/β ratio and the best performance of 5% Ce concentration. To be more quantitative, the α/β ratios are calculated using the proposed model of Eqs. (1)–(5) with only two parameter adjustments. The energy transfer rate, S_T, is measured to be proportional to the Ce concentration. A linear extrapolation of the energy transfer rate is applied based on the 5% Ce situation. Moreover, with the increase of Ce concentration, the probability of the direct excitation of Ce dopant increases as well. The instant excited Ce^{3+} ions, G_{Ce^*}, is assumed the same as the Ce concentration.

The α/β ratio of $LaBr_3$:Ce as a function of cerium concentration, measured with internal ^{215}Po contamination, $E\alpha = 7386$ keV is shown as the black square in Fig. 15. The simulated α/β ratios of a particle with the ionization density of (560×5.1) MeV cm^{-1} are also shown as the red triangles, which shows a reasonably good coincidence with the measurement. A further improvement of the model and the parameters can be carried out in the future with more experimental measurements.

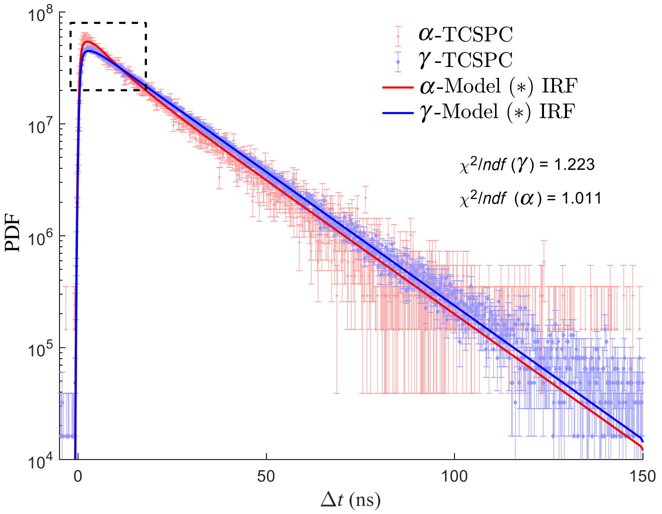

FIG. 14. Summary of α and γ pulse shapes from experiments and model calculations. The blue ones are for the γ rays, while the red ones are for the α particles. The dots are for the measured decay curves with the TCPSC method, while the solid curves are the calculated model results.

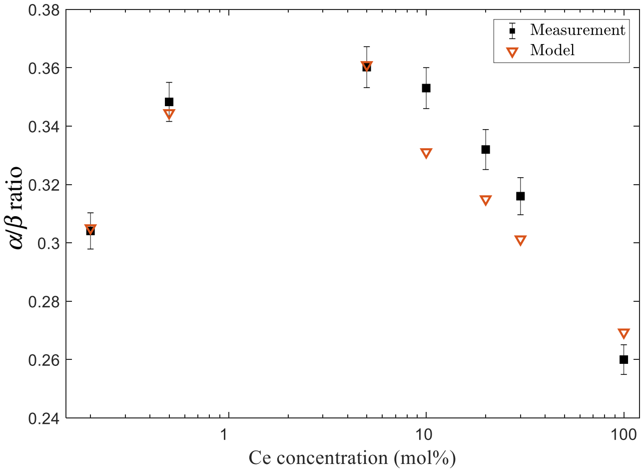

FIG. 15. Comparison of the α/β ratio of $LaBr_3$:Ce between simulation and measurement. The black rectangle points are the α/β ratio of $LaBr_3$:Ce as a function of cerium concentration, measured with internal 215Po contamination, $E\alpha = 7386$ keV. The red triangles are the simulated α/β ratios of a particle with the ionization density of (560×5.1) MeV cm^{-1}.

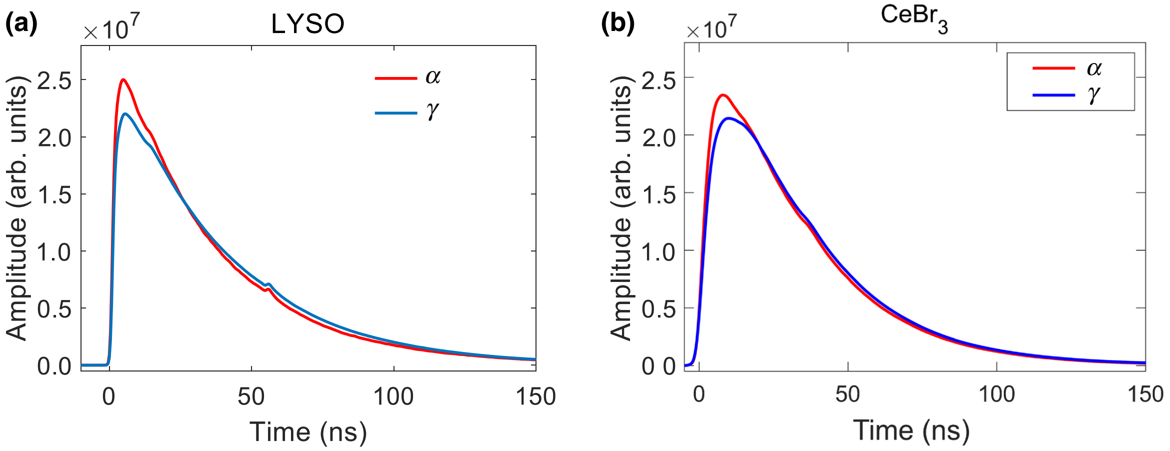

FIG. 16. (a) The averaged pulse shapes of a 5-mm LYSO cube under the excitation of a ^{241}Am source. The blue line is the averaged pulse of the 59.5-keV γ rays, and the red line is the averaged pulse of the α particle. (b) The averaged pulse shapes of a $\phi 51 \times 51$-mm $CeBr_3$ cylinder. The blue line is the averaged pulse of the 1500–2000 keV γ rays, and the red line is the averaged pulse of the α particle.

B. Dopant quenching and the pulse-shape difference of LYSO and $CeBr_3$

LYSO:Ce and $CeBr_3$ are both fast scintillators and normally considered to possess only a single-decay component. The 10%–90% rise time of decay profile is 180 ps and 165 ps for LYSO and $CeBr_3$, respectively [64], which is associated with a certain energy transfer time constant of approximately 80 ps. The average pulse shapes of LYSO, from the direct output of R2083 PMT at 50 Ohm, under excitations of external ^{241}Am-α and ^{22}Na-γ sources are shown in Fig. 16(a). Similarly, the average pulse shapes of $CeBr_3$ measured with internal low-activity ^{227}Ac-α contamination and external ^{22}Na-γ source, are shown in Fig. 16(b).

Due to the very fast rising time of pulse shapes of LYSO and $CeBr_3$, the α and γ pulse-shape difference can not be from the very fast energy-transfer process. The faster decay profiles of the α particles indicate that the quenching between the luminescence centers, probably dopant Ce^{3+} ions, can lead to the pulse-shape differences of such fast scintillators. A detailed and quantitative study of LYSO and $CeBr_3$ on both nonproportionality and the pulse shape will be carried out in the future.

VI. CONCLUSION

It is confirmed that inorganic scintillators with single-decay components also possess the ability of pulse-shape discrimination between α and γ particles, such as $LaBr_3$:Ce^{3+} and LYSO, while the reason for the pulse-shape difference in such single-decay-component scintillators remains unclear. In this paper, coupled rate and transport equations are established, taking typical single-decay-component scintillator $LaBr_3$:Ce^{3+} as an example, to model the whole scintillation processes based on the previous studies on the scintillation mechanism of inorganic scintillators. With one parameter set, most of which can be measured with experiments and simulations, multiple observables of $LaBr_3$:Ce scintillation responses can be reproduced and further explained by the model, including the ionization-density-dependent pulse-shape differences for α or γ particles, the proportionality response of electrons and quenching factor of α particles.

The following conclusions are drawn.

(1) With the quantitative discussion of the parameters and thus their influences on nonproportionality and pulse shape, the quenching process between the excited states of doped ions (Ce^{3+*}) is confirmed to mainly contribute observable ionization-density-dependent α/γ pulse-shape differences of single-decay-component inorganic scintillator $LaBr_3$:Ce.

(2) The model reveals the relation between α quenching factor and Ce concentration in the $LaBr_3$:Ce scintillator, which is in good accordance with previous experiments [55]. It is known that the less quenching of the light yield, the better proportionality and energy resolution the scintillators have. Based on the model simulation, the quenching factor of $LaBr_3$:Ce achieves its maximum with 5% Ce concentration, which provides insight on the best energy resolution of 5% Ce concentration $LaBr_3$:Ce.

(3) Based on the study of the quenching process of excited excitation, the generality of ionization density-dependent pulse-shape differences in other fast single-decay-component inorganic scintillators are predicted, and are observed in LYSO and $CeBr_3$ during our preliminary experiments.

Moreover, this model reveals the ionization-density-dependent correlations between nonproportionality of light yield and scintillation pulse shape, which could provide a theoretical basis for the potential possibility of pulse-by-pulse correction of nonlinear quenching with pulse shapes to achieve a better energy resolution, not only for $LaBr_3$:Ce. And we notice such kinds of corrections are preliminarily explored in CsI:Tl [20,65] and NaI:Tl [65] scintillators recently. The establishment of a more quantitative and accurate model of physical processes will not only help to understand the physical principles of scintillators, improve the crystal engineering, but may also reveal potential alternative methods of particle detection.

ACKNOWLEDGMENTS

This work is supported by the Tsinghua University Initiative Scientific Research Program and the National Natural Science Foundation of China (Grant No. 11961141015).

[1] P. Dorenbos, J. T. M. De Haas, and C. W. E. van Eijk, Non-Proportionality in the scintillation and the energy resolution with scintillation crystals, Ieee T Nucl. Sci. **42**, 6 (1995).

[2] S. A. Payne, N. J. Cherepy, G. Hull, J. D. Valentine, W. W. Moses, and W. Choong, Nonproportionality of scintillator detectors: Theory and experiment, Ieee T Nucl. Sci. **56**, 2506 (2009).

[3] M. Moszyński, Energy resolution and non-proportionality of scintillation detectors – new observations, Radiat. Meas. **45**, 372 (2010).

[4] I. V. Khodyuk and P. Dorenbos, Trends and patterns of scintillator nonproportionality, Ieee T Nucl. Sci. **59**, 3320 (2012).

[5] M. Nikl and A. Yoshikawa, Recent R&D trends in inorganic single-crystal scintillator materials for radiation detection, Adv. Opt. Mater. **3**, 463 (2015).

[6] M. Moszyński, A. Syntfeld-Każuch, L. Swiderski, M. Grodzicka, J. Iwanowska, and P. Sibczyński, Energy resolution of scintillation detectors, Nuclear Instruments and Methods in Physics Research Section A: Accelerators, Spectrometers, Detectors and Associated Equipment **805**, 25 (2016).

[7] J. D. Valentine and B. D. Rooney, Design of a Compton spectrometer experiment for studying scintillator nonlinearity and intrinsic energy resolution, Nuclear Instruments and Methods in Physics Research Section A: Accelerators, Spectrometers, Detectors and Associated Equipment **353**, 37 (1994).

[8] W. S. Choong, K. M. Vetter, W. W. Moses, G. Hull, S. A. Payne, N. J. Cherepy, and J. D. Valentine, Design of a facility for measuring scintillator Non-proportionality, Ieee T Nucl. Sci. **55**, 1753 (2008).

[9] I. V. Khodyuk, J. T. M. de Haas, and P. Dorenbos, Nonproportional response between 0.1-100keV energy by means of highly monochromatic synchrotron X-rays, Ieee T Nucl. Sci. **57**, 1175 (2010).

[10] J. Grim, K. Ucer, A. Burger, P. Bhattacharya, E. Tupitsyn, E. Rowe, V. Buliga, L. Trefilova, A. Gektin, G. Bizarri, *et al.*, Nonlinear quenching of densely excited states in wide-gap solids, Phys. Rev. B **87**, 125117 (2013).

[11] S. A. Payne, W. W. Moses, S. Sheets, L. Ahle, N. J. Cherepy, B. Sturm, S. Dazeley, G. Bizarri, and W. Choong, Nonproportionality of scintillator detectors: Theory and experiment. II, Ieee T Nucl. Sci. **58**, 3392 (2011).

[12] Q. Li, J. Q. Grim, R. T. Williams, G. A. Bizarri, and W. W. Moses, The role of hole mobility in scintillator proportionality, Nuclear Instruments and Methods in Physics Research Section A: Accelerators, Spectrometers, Detectors and Associated Equipment **652**, 288 (2011).

[13] X. Lu, Q. Li, G. A. Bizarri, K. Yang, M. R. Mayhugh, P. R. Menge, and R. T. Williams, Coupled rate and transport equations modeling proportionality of light yield in high-energy electron tracks: CsI at 295 and 100 K; CsI:Tl at 295K, Phys. Rev. B **92**, 115207 (2015).

[14] X. Lu, S. Gridin, R. T. Williams, M. R. Mayhugh, A. Gektin, A. Syntfeld-Kazuch, L. Swiderski, and M. Moszynski, Energy-Dependent scintillation pulse shape and proportionality of decay components for CsI:Tl: Modeling with transport and rate equations, Phys. Rev. Appl. **7**, 14007 (2017).

[15] S. Kerisit, K. M. Rosso, and B. D. Cannon, Kinetic monte carlo model of scintillation mechanisms in CsI and CsI(Tl), Ieee T Nucl. Sci. **55**, 1251 (2008).

[16] Z. Wang, Y. Xie, B. D. Cannon, L. W. Campbell, F. Gao, and S. Kerisit, Computer simulation of electron thermalization in CsI and CsI(Tl), J. Appl. Phys. **110**, 64903 (2011).

[17] D. Åberg, B. Sadigh, A. Schleife, and P. Erhart, Origin of resolution enhancement by co-doping of scintillators: Insight from electronic structure calculations, Appl. Phys. Lett. **104**, 211908 (2014).

[18] M. P. Prange, Y. Xie, L. W. Campbell, F. Gao, and S. Kerisit, Monte carlo simulation of electron thermalization in scintillator materials implications, J. Appl. Phys. **122**, 234504 (2017).

[19] A. Syntfeld-Kazuch, M. M. Ski, A. Widerski, W. Klamra, and A. Nassalski, Light pulse shape dependence on γ-ray energy in CsI, Ieee T Nucl. Sci. **55**, 1246 (2008).

[20] S. Gridin, D. R. Onken, and R. T. Williams, Pulse shape analysis of individual gamma events-correlation to energy resolution and the possibility of its improvement, J. Appl. Phys **124**, 154504 (2018).

[21] C. Hoel, L. G. Sobotka, K. S. Shah, and J. Glodo, Pulse-shape discrimination of La halide scintillators, Nuclear Instruments and Methods in Physics Research Section A: Accelerators, Spectrometers, Detectors and Associated Equipment **540**, 205 (2005).

[22] F. C. L. Crespi, F. Camera, N. Blasi, A. Bracco, S. Brambilla, B. Million, R. Nicolini, L. Pellegri, S. Riboldi, M. Sassi, *et al.*, Alpha–gamma discrimination by pulse shape in $LaBr_3$:Ce and $LaCl_3$:Ce, Nuclear Instruments and Methods in Physics Research Section A: Accelerators, Spectrometers, Detectors and Associated Equipment **602**, 520 (2009).

[23] R. Ogawara and M. Ishikawa, Feasibility study on signal separation for spontaneous alpha decay in LaBr3:Ce

scintillator by signal peak-to-charge discrimination, Rev. Sci. Instrum. **8**, 85108 (2015).

[24] J. E. McFee, C. M. Mosquera, and A. A. Faust, Comparison of model fitting and gated integration for pulse shape discrimination and spectral estimation of digitized lanthanum halide scintillator pulses, Nuclear Instruments and Methods in Physics Research A **828**, 105 (2016).

[25] M. Zeng, J. Cang, Z. Zeng, X. Yue, J. Cheng, Y. Liu, H. Ma, and J. Li, Quantitative analysis and efficiency study of PSD methods for a $LaBr_3$:Ce detector, Nuclear Instruments and Methods in Physics Research Section A: Accelerators, Spectrometers, Detectors and Associated Equipment **813**, 56 (2016).

[26] M. P. Taggart and J. Henderson, Fast-neutron response of $LaBr_3$(Ce) and $LaCl_3$(Ce) scintillators, Nuclear Instruments and Methods in Physics Research Section A: Accelerators, Spectrometers, Detectors and Associated Equipment **975**, 164201 (2020).

[27] H. Cheng, B. Sun, L. Zhu, T. Li, G. Li, C. Li, X. Wu, and Y. Zheng, Intrinsic background radiation of $LaBr_3$(Ce) detector via coincidence measurements and simulations, Nucl. Sci. Tech. **31**, 99 (2020).

[28] T. Alharbi, Pulse-shape discrimination of internal α-contamination in LaBr3:Ce detectors by using the principal component analysis, J. Instrum. **15**, P6010 (2020).

[29] K. Yang and P. R. Menge, in *IEEE Nuclear Science Symposium & Medical Imaging Conference (NSS/MIC)Seattle* (2014).

[30] K. Yang, P. R. Menge, and V. Ouspenski, Enhanced discrimination in Co-doped $LaBr_3$:Ce, Ieee T Nucl. Sci. **63**, 416 (2016).

[31] S. Seifert, J. H. L. Steenbergen, H. T. V. Dam, and D. R. Schaart, Accurate measurements of the rise and decay times of fast scintillators with solid state photon counters, J. Instrum. **7**, P9004 (2012).

[32] Q. Li, J. Q. Grim, K. B. Ucer, A. Burger, G. A. Bizarri, W. W. Moses, and R. T. Williams, Host structure dependence of light yield and proportionality in scintillators in terms of hot and thermalized carrier transport, Physica Status Solidi (RRL) - Rapid Research Letters **6**, 346 (2012).

[33] W. W. Moses, G. A. Bizarri, R. T. Williams, S. A. Payne, A. N. Vasil'Ev, J. Singh, Q. Li, J. Q. Grim, and W. Choong, The origins of scintillator Non-proportionality, Ieee T Nucl. Sci. **59**, 2038 (2012).

[34] K. S. Shah, J. Glodo, M. Klugerman, W. W. Moses, S. E. Derenzo, and M. J. Weber, Labr3:Ce scintillators for gamma-ray spectroscopy, Ieee T Nucl. Sci. **50**, 2410 (2003).

[35] J. Glodo, W. W. Moses, W. M. Higgins, E. V. D. van Loef, P. Wong, S. E. Derenzo, M. J. Weber, and K. S. Shah, Effects of Ce concentration on scintillation properties of $LaBr_3$:Ce, Ieee T Nucl. Sci. **52**, 1805 (2005).

[36] G. Bizarri and P. Dorenbos, Charge carrier and exciton dynamics in $LaBr_3$:Ce^{3+} scintillators: Experiment and model, Phys. Rev. B **75**, 184302 (2007).

[37] M. S. Alekhin, S. Weber, K. W. Krämer, and P. Dorenbos, Optical properties and defect structure of Sr^{2+} co-doped $LaBr_3$:5%Ce scintillation crystals, J. Lumin. **145**, 518 (2014).

[38] P. Li, S. Gridin, K. B. Ucer, and R. T. Williams, Picosecond absorption spectroscopy of self-trapped excitons and transient Ce states in $LaBr_3$ and $LaBr_3$:Ce, Phys. Rev. B **97**, 144303 (2018).

[39] B. Liu, M. Gu, Z. Qi, X. Liu, S. Huang, and C. Ni, First-principles study of lattice dynamics and thermodynamic properties of $LaCl_3$ and $LaBr_3$, Phys. Rev. B **76**, 64307 (2007).

[40] Z. Wang, Y. Xie, L. W. Campbell, F. Gao, and S. Kerisit, Monte carlo simulations of electron thermalization in alkali iodide and alkaline-earth fluoride scintillators, J. Appl. Phys. **112**, 14906 (2012).

[41] I. V. Khodyuk, F. G. A. Quarati, M. S. Alekhin, and P. Dorenbos, Energy resolution and related charge carrier mobility in $LaBr_3$:Ce scintillators, J. Appl. Phys. **114**, 123510 (2013).

[42] G. Bizarri, J. T. M. de Haas, P. Dorenbos, and C. W. E. van Eijk, Scintillation properties of 1 (1 inch $LaBr_3$: 5%Ce^{3+} crystal, Ieee T Nucl. Sci. **53**, 615 (2006).

[43] J. Q. Grim, Q. Li, K. B. Ucer, A. Burger, G. A. Bizarri, W. W. Moses, and R. T. Williams, The roles of thermalized and hot carrier diffusion in determining light yield and proportionality of scintillators, Phys. Status Solidi A **209**, 2421 (2012).

[44] P. Erhart, A. Schleife, B. Sadigh, and D. Aberg, Quasiparticle spectra, absorption spectra, and excitonic properties of NaI and SrI_2 from many-body perturbation theory, Phys Rev B **89**, 75132 (2014).

[45] W. Wolszczak and P. Dorenbos, Shape of intrinsic alpha pulse height spectra in lanthanide halide scintillators, Nuclear Instruments and Methods in Physics Research Section A: Accelerators, Spectrometers, Detectors and Associated Equipment **857**, 66 (2017).

[46] R. M. Van Ginhoven, J. E. Jaffe, S. Kerisit, and K. M. Rosso, Trapping of holes and excitons in scintillators: CsI and LaX_3 (X = Cl, Br), Ieee T Nucl. Sci. **57**, 2303 (2010).

[47] Q. Li, J. Q. Grim, R. T. Williams, G. A. Bizarri, and W. W. Moses, A transport-based model of material trends in nonproportionality of scintillators, J. Appl. Phys. **109**, 123716 (2011).

[48] Zhiguo Wang, Richard T. Williams, Joel Q. Grim, Fei Gao, and Sebastien Kerisit, Kinetic monte carlo simulations of excitation density dependent scintillation in CsI and CsI(Tl), Physica Status Solidi (B) **250**, 1532 (2013).

[49] M. P. Prange, R. M. Van Ginhoven, N. Govind, and F. Gao, Formation, stability, and mobility of self-trapped excitations in NaI and NaI 1-x Tl x from first principles, Phys. Rev. B – Condens. Matter Mater. Physics **87**, 115101 (2013).

[50] P. R. Beck, S. A. Payne, S. Hunter, L. Ahle, N. J. Cherepy, and E. L. Swanberg, Nonproportionality of scintillator detectors. V. comparing the gamma and electron response, Ieee T Nucl. Sci. **62**, 1429 (2015).

[51] R. T. Williams, J. Q. Grim, Q. Li, K. B. Ucer, G. A. Bizarri, and A. Burger, in *Excitonic and Photonic Processes in Materials*, edited by J. Singh, R. T. Williams (Springer, Singapore, 2015), p. 299.

[52] B. D. Rooney and J. D. Valentine, Benchmarking the Compton coincidence technique for measuring electron response non-proportionality in inorganic scintillators, Ieee T Nucl. Sci. **43**, 1271 (1996).

[53] W. Choong, G. Hull, W. W. Moses, K. M. Vetter, S. A. Payne, N. J. Cherepy, and J. D. Valentine, Performance of a facility for measuring scintillator Non-proportionality, Ieee T Nucl. Sci. **55**, 1073 (2008).

[54] I. V. Khodyuk, P. A. Rodnyi, and P. Dorenbos, Nonproportional scintillation response of NaI:Tl to low energy x-ray photons and electrons, J. Appl. Phys. **107**, 113513 (2010).

[55] W. Wolszczak and P. Dorenbos, Nonproportional response of scintillators to alpha particle excitation, Ieee T Nucl. Sci. **64**, 1580 (2017).

[56] A. Jablonski, S. Tanuma, and C. J. Powell, New universal expression for the electron stopping power for energies between 200eV and 30keV, Surf. Interface Anal. **38**, 76 (2006).

[57] G. Bizarri, W. W. Moses, J. Singh, A. N. Vasil'Ev, and R. T. Williams, An analytical model of nonproportional scintillator light yield in terms of recombination rates, J Appl Phys, 105 **105**, 44507 (2009).

[58] F. Gao, S. Kerisit, Y. Xie, D. Wu, M. Prange, R. Van Ginhoven, L. Campbell, and Z. Wang, Science-Driven Candidate Search for New Scintillator Materials FY 2013 Annual Report (2013).

[59] M. S. Alekhin, J. T. M. de Haas, I. V. Khodyuk, K. W. Krämer, P. R. Menge, V. Ouspenski, and P. Dorenbos, Improvement of γ-ray energy resolution of $LaBr_3$:Ce^{3+} scintillation detectors by Sr^{2+} and Ca^{2+} co-doping, Appl. Phys. Lett. **102**, 161915 (2013).

[60] L. M. Bollinger and G. E. Thomas, Measurement of the time dependence of scintillation intensity by a delayed-coincidence method, Rev. Sci. Instrum. **32**, 1044 (1961).

[61] H. T. van Dam, S. Seifert, W. Drozdowski, P. Dorenbos, D. R. Schaart, Optical Absorption Length, and Scattering Length, And refractive index of $LaBr_3$:Ce^{3+}, Ieee T Nucl. Sci. **59**, 656 (2012).

[62] J. Glodo, E. V. van Loef, N. J. Cherepy, S. A. Payne, and K. S. Shah, Concentration effects in Eu doped SrI2, Ieee T Nucl. Sci. **57**, 1228 (2010).

[63] D. N. ter Weele, D. R. Schaart, and P. Dorenbos, The effect of self-absorption on the scintillation properties of Ce^{3+} activated $LaBr_3$ and $CeBr_3$, Ieee T Nucl. Sci. **61**, 683 (2014).

[64] D. N. ter Weele, D. R. Schaart, and P. Dorenbos, Intrinsic scintillation pulse shape measurements by means of picosecond x-ray excitation for fast timing applications, Nuclear Instruments and Methods in Physics Research Section A: Accelerators, Spectrometers, Detectors and Associated Equipment **767**, 206 (2014).

[65] A. Gektin, A. N. Vasil'Ev, V. Suzdal, and A. Sobolev, Energy resolution of scintillators in connection With track structure, Ieee T Nucl. Sci. **67**, 880 (2020).